Exploring the Effects of a High-Order Vertical Coordinate in a Non-Hydrostatic Global Model

Paul A. Ullrich[1] and Jorge E. Guerra[1]

University of California, Davis, Davis, California, USA
paullrich@ucdavis.edu

Abstract
As atmospheric models are pushed towards non-hydrostatic resolutions, there is a growing need for new numerical discretizations that are accurate, robust and effective at these scales. In this paper we describe a new arbitrary-order staggered nodal finite-element method (SNFEM) vertical discretization motivated by flux reconstruction methods. The SNFEM formulation generalizes traditional second-order vertical discretizations, including Lorenz and Charney-Phillips discretizations, to arbitrary order-of-accuracy while preserving desirable properties such as energy conservation. Preliminary results are presented from applying this method to an idealized global baroclinic instability.

Keywords: high-order, atmospheric modeling, non-hydrostatic, vertical coordinate, finite elements

1 Introduction

In typical general circulation models, the Earth's atmosphere is discretized at a horizontal resolution of approximately $25 - 110$ km and a vertical resolution ranging from 100 m in the lowest model levels to $3 - 4$ km near the model top. For fully explicit temporal discretizations, the maximum time-step allowed by these models is restricted the Courant-Friedrichs-Lewy (CFL) condition, which relates the time-step to the spatial resolution via the maximum wave speed. However, the relatively fine grid spacing in the vertical then leads to a substantial restriction on the maximum allowed global time-step size. To overcome this difficulty, the hydrostatic approximation has traditionally been used to enforce instantaneous balance between the vertical pressure gradient force and gravity and so remove vertically propagating sound waves from the system. However, this approximation ignores horizontal transport of vertical velocity and so is no longer valid for horizontal grid resolutions below approximately 10 km.

With horizontal resolutions quickly approaching this limit, the next generation of modeling systems will need to adopt the Naviér-Stokes equations in their unapproximated form. Models using these equations (as opposed to the hydrostatic primitive equations) are typically referred to as non-hydrostatic models. To avoid the bound on the CFL condition due to vertical resolution, work is ongoing on the use of an explicit temporal discretization in the horizontal in

conjunction with an implicit temporal discretization in the vertical (a technique known as Horizontally Explicit Vertically Implicit, HEVI). To retain high-order accuracy, these discretizations are usually coupled via an Implicit-Explicit Runge-Kutta (IMEX-RK) method [3, 29, 30].

Staggered methods are a class of discretizations where scalar (density, pressure and tracer density) and velocity degrees of freedom are stored at different spatial locations [1]. These methods have long been used for both horizontal discretizations in atmospheric models [14, 20, 24] and vertical discretizations [2, 5]. These methods further have excellent dispersive properties and do not support stationary (zero phase speed) $2\Delta x$ modes [15, 25, 27], which are notorious for polluting atmospheric models. Alongside the rise of finite element methods for atmospheric modeling, there has been a renewed interest in pursuing staggering for finite element methods [4, 6, 21] analogous to the mixed-finite element methods employed for elliptic problems [16].

This paper explores a discretization we refer to as **staggered nodal finite element methods (SNFEMs)**, which are a class of arbitrary order-of-accuracy methods that extend traditional nodal finite element methods (NFEMs) by storing scalar and velocity degrees of freedom at differential spatial locations. In particular, this paper focuses on the use of SNFEM for discretization of the model's vertical coordinate. The development of a high-order SNFEM vertical coordinate has the potential to improve simulation quality and reduce pressure gradient errors. To assess this method, we have implemented several SNFEM discretizations within the Tempest framework [28] and are performing an ongoing intercomparison of this formulation with other schemes.

2 The non-hydrostatic equations of fluid motion

Global atmospheric models have traditionally employed the hydrostatic approximation, which assumes that the vertical atmosphere is perpetually in a state of balance between pressure gradient and buoyancy forces. However, this approximation breaks down when the horizontal resolution is finer than roughly 10 km. With high-resolution atmospheric modeling in mind, we will employ the unapproximated non-hydrostatic equations [9]. These equations, with shallow-atmosphere approximation enforced, can be written in an arbitrary coordinate frame (α, β, ξ) as follows:

$$\frac{\partial u^\alpha}{\partial t} + u^i \nabla_i u^\alpha + \theta g^{\alpha i} \nabla_i \Pi + f(\mathbf{k} \times \mathbf{u})^\alpha = 0, \tag{1}$$

$$\frac{\partial u^\beta}{\partial t} + u^i \nabla_i u^\beta + \theta g^{\beta i} \nabla_i \Pi + f(\mathbf{k} \times \mathbf{u})^\beta = 0, \tag{2}$$

$$\frac{\partial \theta}{\partial t} + u^\alpha \frac{\partial \theta}{\partial \alpha} + u^\beta \frac{\partial \theta}{\partial \beta} = -u^\xi \frac{\partial \theta}{\partial \xi}, \tag{3}$$

$$\frac{\partial w}{\partial t} + u^\alpha \nabla_\alpha w + u^\beta \nabla_\beta w + u^\xi \nabla_\xi w = -\theta \left(\frac{\partial r}{\partial \xi} \right)^{-1} \frac{\partial \Pi}{\partial \xi} - g_c, \tag{4}$$

$$\frac{\partial \rho}{\partial t} + \frac{1}{J} \frac{\partial}{\partial \alpha} (J \rho u^\alpha) + \frac{1}{J} \frac{\partial}{\partial \beta} (J \rho u^\beta) = -\frac{1}{J} \frac{\partial}{\partial \xi} (J \rho u^\xi), \tag{5}$$

where summation is implied over $i \in \{\alpha, \beta, \xi\}$ and the coordinate velocity u^ξ is given by

$$u^\xi(w, u^\alpha, u^\beta) = \left(\frac{\partial r}{\partial \xi} \right)^{-1} \left[w - \left(\frac{\partial r}{\partial \alpha} \right) u^\alpha - \left(\frac{\partial r}{\partial \beta} \right) u^\beta \right]. \tag{6}$$

Here α and β are arbitrary horizontal coordinates with basis vectors $\mathbf{g}_\alpha$ and $\mathbf{g}_\beta$, $\xi \in [0,1]$ is a vertical coordinate with basis vector $\mathbf{g}_\xi$ (which is perpendicular to surfaces of constant ξ), $r = r(\alpha,\beta,\xi)$ is the radius in physical coordinates with radial unit vector $\mathbf{k}$, g^{ij} denotes the contravariant metric, $J = \sqrt{\det g_{ij}}$ is the metric Jacobian, g_c is gravity, f is the Coriolis parameter, ρ is the density, $\mathbf{u} = u^\alpha \mathbf{g}_\alpha + u^\beta \mathbf{g}_\beta + u^\xi \mathbf{g}_\xi$ is the vector velocity, θ is the potential temperature and Π is the Exner pressure. Einstein summation notation (implied summation) is used for repeated indices. These equations make use of the covariant derivative ∇_i, which can be expanded as

$$g^{ji}\nabla_i \Pi = g^{j\alpha}\left(\frac{\partial \Pi}{\partial \alpha}\right) + g^{j\beta}\left(\frac{\partial \Pi}{\partial \beta}\right) + g^{j\xi}\left(\frac{\partial \Pi}{\partial \xi}\right), \tag{7}$$

$$u^i \nabla_i u^j = u^\alpha \left(\frac{\partial u^j}{\partial \alpha}\right) + u^\beta \left(\frac{\partial u^j}{\partial \beta}\right) + u^\xi \left(\frac{\partial u^j}{\partial \xi}\right) + \Gamma^j{}_{ik} u^i u^k, \tag{8}$$

$$u^i \nabla_i w = u^\alpha \left(\frac{\partial w}{\partial \alpha}\right) + u^\beta \left(\frac{\partial w}{\partial \beta}\right) + u^\xi \left(\frac{\partial w}{\partial \xi}\right), \tag{9}$$

where $\Gamma^j{}_{ik}$ denotes the Christoffel symbols of the second kind associated with the coordinate transform (again with summation over repeated indices i and k implied). Further, the Coriolis term can be written as

$$(\mathbf{k} \times \mathbf{u})^\alpha = g^{\alpha\beta}\epsilon_{\beta r \alpha} u^\alpha + g^{\alpha\alpha}\epsilon_{\alpha r \beta} u^\beta = J\left[g^{\alpha\beta}u^\alpha - g^{\alpha\alpha}u^\beta\right], \tag{10}$$

$$(\mathbf{k} \times \mathbf{u})^\beta = g^{\beta\beta}\epsilon_{\beta r \alpha} u^\alpha + g^{\beta\alpha}\epsilon_{\alpha r \beta} u^\beta = J\left[g^{\beta\beta}u^\alpha - g^{\beta\alpha}u^\beta\right]. \tag{11}$$

The non-hydrostatic equations are closed via the equation of state

$$\Pi(\rho,\theta) = c_p \left(\frac{p_0}{p}\right)^{R_d/c_p} = c_p \left(\frac{R_d \rho \theta}{p_0}\right)^{R_d/c_v} \tag{12}$$

where R_d is the ideal gas constant for dry air, p_0 is a reference pressure and c_p and c_v denote the specific heat capacity of dry air at constant pressure and constant volume. Observe that (1)-(4) are given in a non-conservative form; this formulation is generally desirable over the conservative formulation (where momentum and $\rho\theta$ are prognostic variables) since this form can more readily conserve quantities relevant to atmospheric motion, such as total energy, angular momentum and potential enstrophy, and (depending on the discretization) can lead to a more accurate treatment of wave-like motions [25].

Note that the equations above use w as a prognostic variable in place of u^ξ. This choice has the advantage of avoiding several complicated metric terms which arise in the evolution equation of u^ξ, at the cost of introducing an additional diagnostic equation for the coordinate velocity (6). Imperfect balance of these additional geometric terms has been observed to cause the generation of a spurious wave mode, analogous to the observation of [13].

The equations (1)-(4) do not specify a coordinate system and so can be used for either Cartesian or spherical geometry, only depending on the specification of the three geometric quantities: the metric Jacobian J, the contravariant metric g^{ij} and the Christoffel symbols of the second kind $\Gamma^i{}_{jk}$.

To account for topography, terrain-following σ-coordinates are imposed by defining the radius $r = r(\alpha,\beta,\xi)$ so that $r(\alpha,\beta,0)$ is coincident with the surface. For simplicity, we will

employ Gal-Chen and Somerville coordinates [8], which arise from the choice

$$r(\alpha, \beta, \xi) = \xi \left[z_{top} - z_s(\alpha, \beta) \right] + a + z_s(\alpha, \beta), \tag{13}$$

where a is the radius of the Earth, z_{top} denotes the model height and $z_s(\alpha, \beta)$ denotes the surface elevation.

3 Discretization

The computational domain consists of n_l model levels and $n_l + 1$ model interfaces, which are staggered in the vertical direction. Throughout this manuscript we will use subscript n to denote variables stored on model levels and subscript i to denote variables stored on interfaces. Although the exact placement of levels and interfaces is at the discretion of the model developer, we choose to divide the vertical into n_{ve} vertical nodal finite elements with n_{vp} levels per element. Levels are placed at Gaussian quadrature nodes and interfaces at Gauss-Lobatto quadrature nodes.

The placement of prognostic variables follows [25, 23, 26], who argue that there is only one possible arrangement that maintains optimal wave propagation properties, avoids computational modes and allows for mass to be readily conserved. Specifically, under this formulation, variables ρ, u and v are stored on model levels and w and θ are stored on model interfaces.

For simplicity, we employ the Strang-Carryover IMEX-RK scheme for the temporal discretization [29]. The vertical implicit solver has been implemented with three solution methods: an iterative GMRES-type solver, a generalized matrix solver based on the `DGESV` solver from LAPACK, and a diagonal matrix solver based on the `DGBSV` solver from LAPACK.

3.1 Vertical Discretization

Discrete evolution equations for the vertically staggered variables are constructed using an approach similar to flux reconstruction [11, 28]. Under this formulation, an interpolating polynomial over nodal values is first constructed within an element. Values and derivatives of the polynomial are then evaluated where necessary, augmented (when a discontinuity exists in the reconstruction at element edges) by the robust derivative operator [28]. A depiction of the vertical differentiation procedure is given in Figure 1. Continuity is enforced via direct stiffness summation [18].

Quantitatively, this discretization requires the construction of interpolation operators $\mathcal{I}_i^n$ and $\mathcal{I}_n^i$ which represent interpolation from nodes to interfaces and interfaces to nodes, respectively. We also require differentiation operators from interfaces to interfaces ($\mathcal{D}_i^i$), from interfaces to levels ($\mathcal{D}_n^i$), levels to levels ($\mathcal{D}_n^n$) and levels to interfaces ($\mathcal{D}_i^n$). The first two operators ($\mathcal{D}_i^i$ and $\mathcal{D}_n^i$) are defined simply by differentiating the interpolating polynomials from model interfaces, and averaging at element boundaries. This is effectively a weak differentiation operation since the interpolating polynomials of the interface variables is C^0.

However, differentiation from levels to levels ($\mathcal{D}_n^n$) and levels to interfaces ($\mathcal{D}_i^n$) requires additional augmentation since the interpolating polynomials over levels are discontinuous at element edges. To proceed, a robust differentiation operator is constructed. Define $\mathcal{Z} = [\xi_{j,0}, \xi_{j,n_{vp}-1}]$ as the closed interval representing a single vertical element, with boundary $\partial\mathcal{Z}$. Let $f : \xi \to \mathbb{R}$ be the interpolating polynomial on levels, which is defined and continuous on $\mathcal{Z} \cup \partial\mathcal{Z}$. Further, let $\tilde{f} : \xi \to \mathbb{R}$, representing the values of the interpolating polynomial on levels in adjacent elements, be defined on $\partial\mathcal{Z}$. If continuity were enforced then one would expect that f and $\tilde{f}$

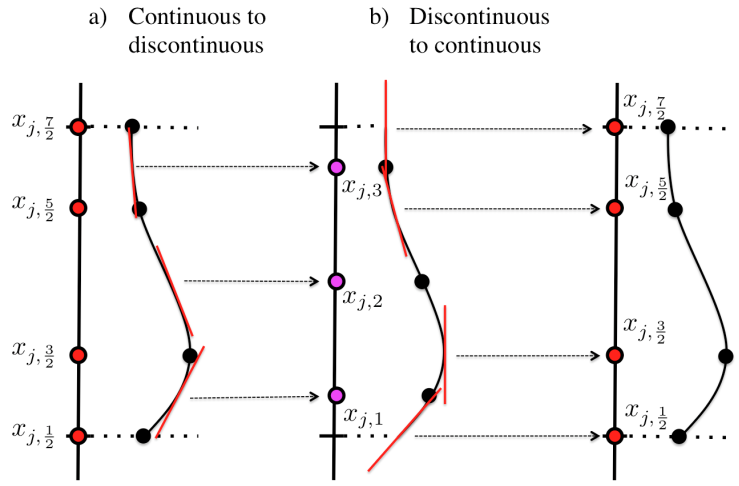

Figure 1: A depiction of the differentiation procedure linking variables stored at continuous (red) and discontinuous (purple) nodes. (a) For interpolation/differentiation of continuous variables needed at discontinuous nodes the continuous polynomial interpolant is simply evaluated / differentiated at each node. (b) For interpolants derivatives of discontinuous variables needed at continuous nodes, the robust differentiation procedure is used.

must satisfy $\tilde{f}(\alpha,\beta) = f(\alpha,\beta)$ on $\partial\mathcal{Z}$, but in this case no such criteria is enforced. Following [11], robust differentiation in the ξ direction is defined via

$$D_\xi f(\xi_{j,i}) = \left.\frac{\partial f}{\partial \xi}\right|_{\xi=\xi_{j,i}} + \frac{dg_R}{d\xi}(\xi_{j,i})(\overline{f}_{(n_{vp}-1,j)} - f_{(n_{vp}-1,j)}) + \frac{dg_L}{d\xi}(\xi_{j,i})(\overline{f}_{(0,j)} - f_{(0,j)}), \quad (14)$$

where the overline denotes the co-located average of f and $\tilde{f}$,

$$\overline{f}_{(j,n_{vp}-1)} = \frac{f(\xi_{j,n_{vp}-1}) + \tilde{f}(\xi_{j,n_{vp}-1})}{2}, \qquad \overline{f}_{(0)} = \frac{f(\xi_{j,0}) + \tilde{f}(\xi_{j,0})}{2}. \quad (15)$$

Here g_L and g_R are the local *flux correction functions*, which are chosen to satisfy

$$g_L(\xi_{j,0}) = 1, \qquad g_L(\xi_{j,n_{vp}-1}) = 0, \qquad g_R(\xi_{j,0}) = 0, \qquad g_R(\xi_{j,n_{vp}-1}) = 1, \quad (16)$$

and otherwise are chosen to approximate zero throughout $[\alpha_0, \alpha_{n_{vp}-1}]$. Options for g_L and g_R include g_1 (Radau polynomials), which will lead to the discontinuous Galerkin method, and g_2, which will lead to the mass-lumped discontinuous Galerkin method. For the remainder of this text we will adopt the mass-lumped functions g_2, as described in [11]. These correction functions are exactly zero at Gauss-Lobatto nodes within an element, and so lead to a simplification of the correction terms when evaluated at model interfaces.

A description of the numerical implementation of this method now follows. Here we use boldface to represent variables stored in a column. Algorithmically, Exner pressure is first

computed on model levels via

$$\boldsymbol{\Pi}_n \approx c_p \left(\frac{R_d \boldsymbol{\rho}_n}{p_0} \right)^{R_d/c_v} \left(\mathcal{I}_n^i \boldsymbol{\theta}_i \right)^{R_d/c_v}, \tag{17}$$

and mass flux is computed on model interfaces via

$$\boldsymbol{F}_i \approx J_{k+1/2} \left(\mathcal{I}_i^n \boldsymbol{\rho}_n \right) u^\xi_{k+1/2}. \tag{18}$$

At the top and bottom interface F_i must be set to zero in order to enforce mass conservation. The right-hand-side terms of (1)-(5) are then discretized as follows:

$$-u^\xi \frac{\partial \theta}{\partial \xi}\bigg|_i \approx -\boldsymbol{u}_i^\xi \mathcal{D}_i^i \boldsymbol{\theta}_i, \tag{19}$$

$$-\theta \left(\frac{\partial r}{\partial \xi} \right)^{-1} \frac{\partial \Pi}{\partial \xi} - g_c \bigg|_i \approx -\boldsymbol{\theta}_i \left(\frac{\partial r}{\partial \xi} \right)^{-1} \mathcal{D}_i^n \boldsymbol{\Pi}_n - g_c, \tag{20}$$

$$-\frac{1}{J} \frac{\partial F}{\partial \xi}\bigg|_n \approx \frac{1}{J_k} \mathcal{D}_n^i \boldsymbol{F}_i. \tag{21}$$

At the top and bottom interface, (19) and (20) are set to zero.

Vertical advection of velocity is handled in an analogous manner. First u^ξ is computed on model levels,

$$\mathbf{u}_n^\xi \approx \left(\frac{\partial r}{\partial \xi} \right)_n^{-1} \left[\mathcal{I}_n^i \mathbf{w}_i - \left(\frac{\partial r}{\partial \alpha} \right)_n \mathbf{u}_n^\alpha - \left(\frac{\partial r}{\partial \beta} \right)_n \mathbf{u}_n^\beta \right], \tag{22}$$

and on model interfaces,

$$\mathbf{u}_i^\xi \approx \left(\frac{\partial r}{\partial \xi} \right)_{k+1/2}^{-1} \left[\mathbf{w}_i - \left(\frac{\partial r}{\partial \alpha} \right)_{k+1/2} \mathcal{I}_i^n \mathbf{u}_n^\alpha - \left(\frac{\partial r}{\partial \beta} \right)_i \mathcal{I}_i^n \mathbf{u}_n^\beta \right]. \tag{23}$$

Note that the advected terms in this formulation are susceptible to stationary $2\Delta x$ modes, regardless of the order of accuracy of the underlying discretization [27]. Consequently, the development of an effective scheme for upwinding in the vertical within the SNFEM framework is desirable and an area of ongoing work.

3.2 Horizontal Discretization

Spherical shells are discretized in the horizontal using an equiangular cubed-sphere grid [19, 17], which consists of six Cartesian patches arranged along the faces of a inflated cube [28]. On the equiangular cubed-sphere grid, coordinates are given as (α, β, p), with central angles $\alpha, \beta \in [-\frac{\pi}{4}, \frac{\pi}{4}]$ and panel index $p \in \{1, 2, 3, 4, 5, 6\}$. By convention, we choose panels 1–4 to be along the equator and panels 5 and 6 to be centered on the northern and southern pole, respectively. With uniform grid spacing, each panel consists of a square array of $n_e \times n_e$ elements with global polynomial order n_p. The horizontal discretization otherwise follows the continuous spectral element formulation [28], analogous to earlier efforts with spectral elements [10, 7, 22, 9].

4 Validation: Baroclinic Instability

The baroclinic instability test of [12] is an important test case for hydrostatic dynamical cores. Although it does not describe a non-hydrostatic phenomena, it represents a first mechanism to validate global atmospheric model performance; in particular, we would expect that a correct and validated non-hydrostatic model should produce results analogous to those of a hydrostatic model (for which many reference solutions are available). The background field is chosen to qualitatively resemble the real atmosphere. A small exponential-type perturbation is then added which triggers the generation of an instability. Initialization of this test case in height coordinates follows an iterative procedure [12].

The temperature T is computed in terms of the density and potential temperature using (12) and the ideal gas law,

$$T(\rho,\theta) = \frac{p_0}{\rho R_d}\left(\frac{R_d \rho \theta}{p_0}\right)^{c_p/c_v}$$

Three simulations were conducted on a small computing cluster with a fixed horizontal grid resolution of $n_e = 30$ and $n_p = 4$ (corresponding to $48,602$ degrees of freedom per variable per model level or 110 km equatorial resolution), $n_l = 30$ and a 30 km model cap. The time step was fixed at $\Delta t = 240$ s. For each simulation the vertical polynomial order is varied by choosing $n_{vp} = \{1, 3, 30\}$ keeping the total number of degrees of freedom constant. Computational performance did not vary significantly between simulations, with the high-order $n_{vp} = 30$ case associated with approximately a 10% slowdown compared with the $n_{vp} = 1$ case. Models typically use a stretched vertical coordinate in order to improve vertical resolution near the surface, where the strongest vertical gradients in the baroclinic instability are present. However, in this case we purposefully use uniformly spaced elements, leading to under-resolution of the vertical in order to emphasize the effect of vertical order-of-accuracy on the development of the instability.

Surface temperature and surface pressure from these simulations are depicted in Figure 2 over the region of instability. The vertical coordinate with centered differences (1 level per element) produces a baroclinic instability with the correct structure but relatively weak central pressure. Increasing the number of levels per element leads to a similar structure, but a greatly improved central pressure. This formulation is further extended to one finite element in the vertical direction, corresponding to 30 levels per element. In this limit we observe that the resulting wave is visually similar to other empirically derived solutions for the baroclinic instability [12].

5 Conclusions

We have described a new method for discretization of the vertical coordinate for atmospheric models based on staggered nodal finite element methods and validated the method using the baroclinic instability state of [12]. The SNFEM formulation herein generalizes traditional second-order vertical discretizations, including Lorenz and Charney-Phillips discretizations, to arbitrary order-of-accuracy while preserving desirable properties such as energy conservation. Improvements in the vertical order of accuracy have been shown to lead to clear improvement in the horizontal structure of the instability at fixed horizontal resolution.

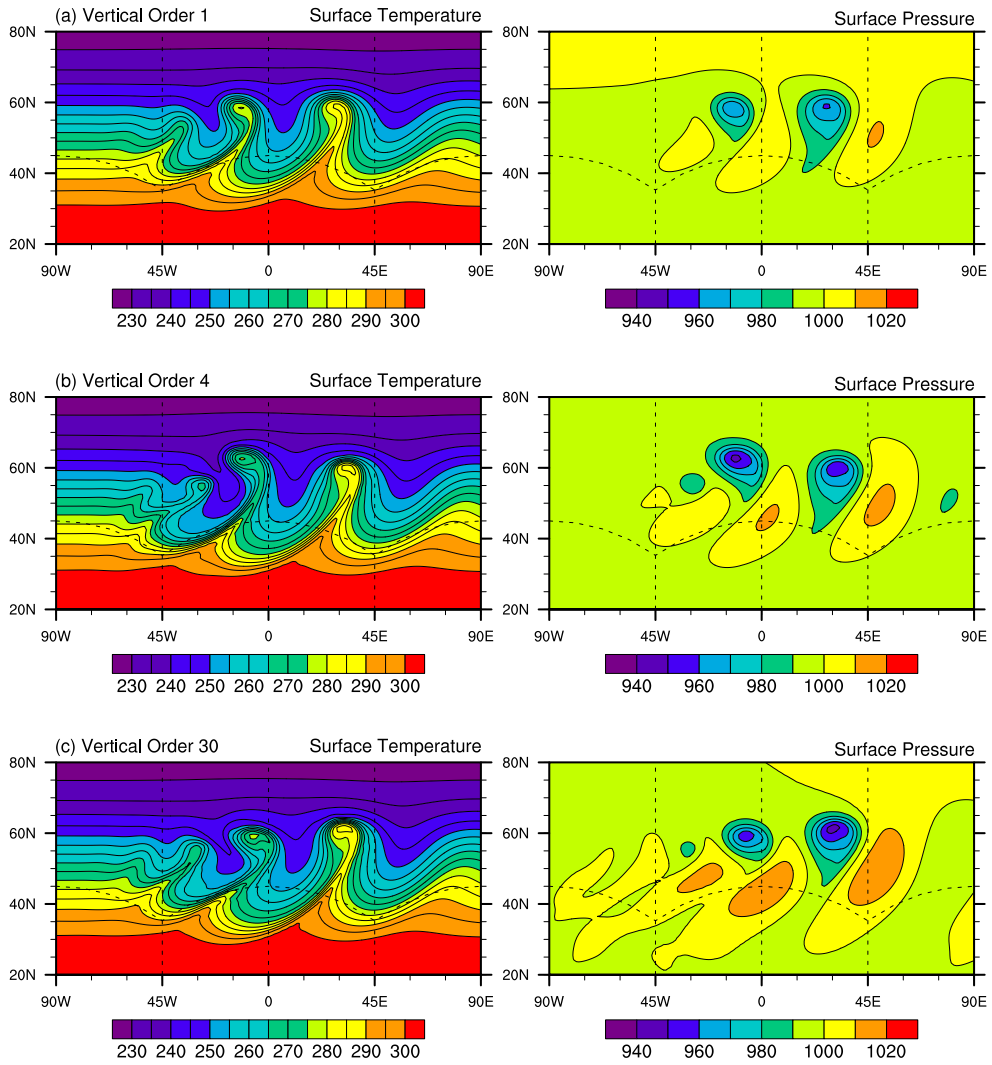

Figure 2: Snapshots from the baroclinic wave test case at day 9 simulated on a n_e30 grid with 30 vertical levels and 30 kilometer model cap. The time step is chosen to be $\Delta t = 240$ s. Surface temperature and pressure are plotted in the left and right columns, respectively. The rows represent (from top to bottom) 1, 3 and 30 levels per element.

References

[1] A. Arakawa and V.R. Lamb. Computational design of the basic dynamical processes of the UCLA general circulation model. *General circulation models of the atmosphere.(A 78-10662 01-47) New York, Academic Press, Inc.*, pages 173–265, 1977.

[2] A. Arakawa and S. Moorthi. Baroclinic instability in vertically discrete systems. *J. Atmos. Sci.*, 45(11):1688–1708, 1988.

[3] U.M. Ascher, S.J. Ruuth, and R.J. Spiteri. Implicit-explicit Runge-Kutta methods for time-dependent partial differential equations. *Appl. Numer. Math.*, 25(2-3):151–167, 1997.

[4] D. Boffi and L. Gastaldi. Some remarks on quadrilateral mixed finite elements. *Comput. Struct.*, 87(11-12):751–757, 2009.

[5] J. G. Charney and N. A. Phillips. Numerical integration of the quasi-geostrophic equations for barotropic and simple baroclinic flows. *J. Atmos. Sci.*, 10:71–99, 1953.

[6] C. J. Cotter and J. Shipton. Mixed finite elements for numerical weather prediction. *J. Comput. Phys.*, 231(21):7076–7091, August 2012.

[7] J. Dennis, J. Edwards, K. J. Evans, O. N. Guba, P. H. Lauritzen, A. A. Mirin, A. St-Cyr, M. A. Taylor, and P. H. Worley. CAM-SE: A scalable spectral element dynamical core for the Community Atmosphere Model. *Int. J. High Perform. Comput. Appl.*, 2011.

[8] T. Gal-Chen and R. C. J. Somerville. On the use of a coordinate transformation for the solution of the Navier-Stokes equations. *J. Comput. Phys.*, 17:209–228, 1975.

[9] F. X. Giraldo, J. F. Kelly, and E. M. Constantinescu. Implicit-explicit formulations of a three-dimensional nonhydrostatic unified model of the atmosphere (NUMA). *SIAM Journal on Scientific Computing*, 35(5):B1162–B1194, 2013.

[10] F. X. Giraldo and T. E. Rosmond. A scalable Spectral Element Eulerian Atmospheric Model (SEE-AM) for NWP: Dynamical core tests. *Mon. Weather Rev.*, 132:133–153, 2004.

[11] H. T. Huynh. A flux reconstruction approach to high-order schemes including discontinuous Galerkin methods. *AIAA paper*, 4079:2007, 2007.

[12] C. Jablonowski and D. L. Williamson. A baroclinic instabilitiy test case for atmospheric model dynamical cores. *Quart. J. Roy. Meteor. Soc.*, 132(621C):2943–2975, 2006.

[13] J. B. Klemp, W. C. Skamarock, and O. Fuhrer. Numerical Consistency of Metric Terms in Terrain-Following Coordinates. *Mon. Weather Rev.*, 131:1229–1239, 2003.

[14] S.-J. Lin. A vertically lagrangian finite-volume dynamical core for global models. *Mon. Weather Rev.*, 132(10):2293–2307, 2004.

[15] D. A. Randall. Geostrophic adjustment and the finite-difference shallow-water equations. *Mon. Weather Rev.*, 122:1371, 1994.

[16] P. Raviart and J. Thomas. A mixed finite element method for 2-nd order elliptic problems. *Mathematical Aspects of Finite Element Methods*, pages 292–315, 1977.

[17] C. Ronchi, R. Iacono, and P. S. Paolucci. The "cubed sphere": A new method for the solution of partial differential equations in spherical geometry. *J. Comput. Phys.*, 124(1):93–114, 1996.

[18] E. M. Rønquist and A. T. Patera. Spectral element multigrid. i. formulation and numerical results. *J. Sci. Comput.*, 2(4):389–406, 1987.

[19] R. Sadourny. Conservative finite-difference approximations of the primitive equations on quasi-uniform spherical grids. *Mon. Weather Rev.*, 100:136–144, 1972.

[20] W. C. Skamarock, J. B. Klemp, M. G. Duda, L. D. Fowler, S.-H. Park, and T. D. Ringler. A multiscale nonhydrostatic atmospheric model using centroidal Voronoi tesselations and C-grid staggering. *Mon. Weather Rev.*, 140:3090–3105, 2012.

[21] A. Staniforth, T. Melvin, and C. Cotter. Analysis of a mixed finite-element pair proposed for an atmospheric dynamical core. *Quart. J. Royal Meteor. Soc.*, 139(674):1239–1254, 2013.

[22] M. A. Taylor and A. Fournier. A compatible and conservative spectral element method on unstructured grids. *J. Comput. Phys.*, 229(17):5879 – 5895, 2010.

[23] J Thuburn. Vertical discretizations giving optimal representation of normal modes: Sensitivity to the form of the pressure-gradient term. *Quart. J. Royal Meteor. Soc.*, 132(621):2809–2825, 2006.

[24] J. Thuburn, T. D. Ringler, W. C. Skamarock, and J. B. Klemp. Numerical representation of geostrophic modes on arbitrarily structured C-grids. *J. Comput. Phys.*, 228(22):8321–8335, 2009.

[25] J. Thuburn and T.J. Woollings. Vertical discretizations for compressible Euler equation atmospheric models giving optimal representation of normal modes. *J. Comput. Phys.*, 203(2):386–404, 2005.

[26] M. D. Toy and D. A. Randall. Comment on the article "Vertical discretizations for compressible Euler equation atmospheric models giving optimal representation of normal modes" by Thuburn and Woollings. *J. Comput. Phys*, 223(1):82–88, 2007.

[27] P. A. Ullrich. Understanding the treatment of waves in atmospheric models, Part I: The shortest resolved waves of the 1D linearized shallow water equations. *Quart. J. Royal Meteor. Soc.*, 140:1426–1440, 2013.

[28] P. A. Ullrich. A global finite-element shallow-water model supporting continuous and discontinuous elements. *Geosci. Model Dev. Disc.*, 7(4):5141–5182, 2014.

[29] P. A. Ullrich and C. Jablonowski. Operator-split Runge-Kutta-Rosenbrock methods for nonhydrostatic atmospheric models. *Mon. Weather Rev.*, 140:1257–1284, 2012.

[30] H. Weller, S.-J. Lock, and N. Wood. Runge–Kutta IMEX schemes for the Horizontally Explicit/Vertically Implicit (HEVI) solution of wave equations. *J. Comput. Phys.*, 252:365–381, 2013.